

Cite this: *Chem. Sci.*, 2020, 11, 2716

All publication charges for this article have been paid for by the Royal Society of Chemistry

# Facile *in situ* reductive synthesis of both nitrogen deficient and protonated g-C<sub>3</sub>N<sub>4</sub> nanosheets for the synergistic enhancement of visible-light H<sub>2</sub> evolution†

Weisong Li,<sup>ab</sup> Zheng Guo,<sup>a</sup> Litong Jiang,<sup>bc</sup> Lei Zhong,<sup>a</sup> Guoning Li,<sup>a</sup> Jiajun Zhang,<sup>a</sup> Kai Fan,<sup>a</sup> Sergio Gonzalez-Cortes,<sup>id</sup><sup>a</sup> Kuijuan Jin,<sup>c</sup> Chunjian Xu,<sup>id</sup><sup>\*a</sup> Tiancun Xiao<sup>\*b</sup> and Peter P. Edwards<sup>id</sup><sup>\*b</sup>

A new strategy is reported here to synthesize both nitrogen deficient and protonated graphitic carbon nitride (g-C<sub>3</sub>N<sub>4</sub>) nanosheets by the conjoint use of NH<sub>4</sub>Cl as a dynamic gas template together with hypophosphorous acid (H<sub>3</sub>PO<sub>2</sub>) as a doping agent. The NH<sub>4</sub>Cl treatment allows for the scalable production of protonated g-C<sub>3</sub>N<sub>4</sub> nanosheets. With the corresponding co-addition of H<sub>3</sub>PO<sub>2</sub>, nitrogen vacancies, accompanied by both additional protons and interstitially-doped phosphorus, are introduced into the g-C<sub>3</sub>N<sub>4</sub> framework, and the electronic bandgap of g-C<sub>3</sub>N<sub>4</sub> nanosheets as well as their optical properties and hydrogen-production performance can be precisely tuned by careful adjustment of the H<sub>3</sub>PO<sub>2</sub> treatment. This conjoint approach thereby results in improved visible-light absorption, enhanced charge-carrier separation and a high H<sub>2</sub> evolution rate of 881.7 μmol h<sup>-1</sup> achieved over the H<sub>3</sub>PO<sub>2</sub> doped g-C<sub>3</sub>N<sub>4</sub> nanosheets with a corresponding apparent quantum yield (AQY) of 40.4% (at 420 nm). We illustrate that the synergistic H<sub>3</sub>PO<sub>2</sub> doping modifies the layered g-C<sub>3</sub>N<sub>4</sub> materials by introducing nitrogen vacancies as well as protonating them, leading to significant photocatalytic H<sub>2</sub> evolution enhancements, while the g-C<sub>3</sub>N<sub>4</sub> materials doped with phosphoric acid (H<sub>3</sub>PO<sub>4</sub>) are simply protonated further, revealing the varied doping effects of phosphorus having different (but accessible) valence states.

Received 8th October 2019  
Accepted 31st January 2020

DOI: 10.1039/c9sc05060d

rsc.li/chemical-science

## Introduction

Graphitic carbon nitride (g-C<sub>3</sub>N<sub>4</sub>), a prototypical metal-free semiconductor, has been intensively studied owing to its excellent photocatalytic applications in H<sub>2</sub> production, environment remediation, CO<sub>2</sub> reduction and photosynthesis.<sup>1–5</sup> Bulk g-C<sub>3</sub>N<sub>4</sub> with high thermal, chemical and photocatalytic stabilities can be readily synthesized *via* direct thermal polymerization of nitrogen-rich precursors. However, the visible-light photocatalytic efficiency of such directly polymerized g-C<sub>3</sub>N<sub>4</sub> material is far from satisfactory stemming from its limited visible-light absorption range, low surface area, confined active sites, and rapid charge-carrier recombination. Thus, various techniques including morphology engineering,<sup>6,7</sup> constructing Z-scheme heterostructure or unique surface bonding states,<sup>8–10</sup>

doping with both nonmetal and metal elements,<sup>11,12</sup> introducing elemental defects or vacancies and protonation have been applied in order to improve the photocatalytic performance of g-C<sub>3</sub>N<sub>4</sub>.<sup>13–15</sup> Inspired by the two-dimensional graphene-like nanosheet of the material, efforts have also been made to transform bulk g-C<sub>3</sub>N<sub>4</sub> into porous structures composing thin nanosheets which help deliver superior photocatalytic activities.<sup>7</sup>

Recently, it has been demonstrated that the photocatalytic activity of g-C<sub>3</sub>N<sub>4</sub> under visible-light irradiation can be significantly enhanced by introducing nitrogen defects into the basic g-C<sub>3</sub>N<sub>4</sub> “melon” structure as well as doping with compounds of phosphorus.<sup>2,12</sup> To date, nitrogen deficient g-C<sub>3</sub>N<sub>4</sub> was synthesized through alkali-assisted polymerization, hydrogen reduction, high-temperature thermal polymerization and hydrothermal routes.<sup>2,13,16,17</sup> Unlike other methods-which routinely suffer from control difficulties-the so-called alkali-assisted polymerization achieves a highly effective control of both the type and the abundance of the introduced nitrogen defects leading to enhanced photocatalytic H<sub>2</sub> evolution.<sup>2</sup> However, this alkali-assisted approach, using KOH, NaOH or Ba(OH)<sub>2</sub> is unlikely to work in the “bottom-up” strategy which utilizes NH<sub>4</sub>Cl as a so-called dynamic gas template for scalable

<sup>a</sup>School of Chemical Engineering & Technology, State Key Laboratory of Chemical Engineering, Tianjin University, Tianjin 300350, China. E-mail: cjxu@tju.edu.cn

<sup>b</sup>Inorganic Chemistry Laboratory, University of Oxford, South Parks Road, Oxford, OX1 3QR, UK. E-mail: xiao.tiancun@chem.ox.ac.uk; peter.edwards@chem.ox.ac.uk

<sup>c</sup>Institute of Physics, Chinese Academy of Sciences, Beijing 100190, China

† Electronic supplementary information (ESI) available: Sample characterization, H<sub>2</sub> evolution equipment, supplementary XRD, XPS and elemental mapping data, photocatalytic H<sub>2</sub> evolution experimental results. See DOI: 10.1039/c9sc05060d



production of g-C<sub>3</sub>N<sub>4</sub> nanosheets, due to the non-coexistence of NH<sub>4</sub>Cl and alkali metal hydroxides.<sup>7</sup> Moreover, it has been shown that the alkali-assisted process progressively decreases the layer stacking distance and reduces the specific surface area of g-C<sub>3</sub>N<sub>4</sub> nanosheets when excessive KOH is added.<sup>2</sup> This suggests the over-addition of alkali metal hydroxides would cause a severe decrease in photocatalytic activity because of the unfavorable crystal morphology changes.

Phosphorus, has emerged as a likely contender to be introduced into the g-C<sub>3</sub>N<sub>4</sub> matrix to achieve enhanced photocatalytic performance. In most of the prior work,<sup>15,18–20</sup> pentavalent phosphorus such as H<sub>3</sub>PO<sub>4</sub>, (NH<sub>4</sub>)<sub>3</sub>PO<sub>4</sub>, BmimPF<sub>6</sub> ionic liquid, Na<sub>2</sub>HPO<sub>4</sub>, and CO(NH<sub>2</sub>)<sub>2</sub>·H<sub>3</sub>PO<sub>4</sub> figures strongly as the phosphorus doping agents. To the best of our knowledge, there is little work reported on the synthesis of phosphorus-doped g-C<sub>3</sub>N<sub>4</sub> using phosphorus compounds having lower valence states and the photocatalytic ability of such low-valent phosphorus doped g-C<sub>3</sub>N<sub>4</sub> has hardly been studied.<sup>4</sup>

Here, we present a one-step, *in situ* reduction method utilizing the strategy of using NH<sub>4</sub>Cl as dynamic gas template and H<sub>3</sub>PO<sub>2</sub> doping for the synthesis of nitrogen deficient g-C<sub>3</sub>N<sub>4</sub> nanosheets. The photocatalytic activity of g-C<sub>3</sub>N<sub>4</sub> was greatly enhanced with the formation of both protonated and porous nanosheets by using NH<sub>4</sub>Cl as dynamic gas template. With the co-addition of H<sub>3</sub>PO<sub>4</sub> as dopant, g-C<sub>3</sub>N<sub>4</sub> nanosheets were further protonated and delivered superior photocatalytic activities. However, besides protonation, the g-C<sub>3</sub>N<sub>4</sub> nanosheets doped by the lower-valent phosphorus compound H<sub>3</sub>PO<sub>2</sub> also led to a reduced electronic bandgap in the material and enhanced visible light absorption. The differences observed between the H<sub>3</sub>PO<sub>2</sub> and H<sub>3</sub>PO<sub>4</sub> doped g-C<sub>3</sub>N<sub>4</sub> nanosheets promotes a discussion of using dopants with phosphorus at different valence states. It demonstrates the possibility of using low-valent phosphorus compounds to both synthesize and modify g-C<sub>3</sub>N<sub>4</sub> in one single step, thereby offering a comprehensive enhanced and efficient visible-light photocatalytic performance. Thus, the preparation strategy reported here represents an effective approach to optimize the morphology, chemical composition, optical response and resulting activity of g-C<sub>3</sub>N<sub>4</sub> photocatalysts.

## Experimental

The standard bulk g-C<sub>3</sub>N<sub>4</sub> reference (B-CN) was prepared by the direct pyrolysis polymerization of dicyandiamide. Preliminary, 4 g dicyandiamide powder was placed in a 50 mL alumina crucible with cover and then was calcined in static air at 550 °C for 4.5 hours with a ramping rate of 2.3 °C min<sup>-1</sup>. The g-C<sub>3</sub>N<sub>4</sub> nanosheets were prepared by the modified “bottom-up” strategy with NH<sub>4</sub>Cl as dynamic gas template,<sup>7</sup> and the as prepared g-C<sub>3</sub>N<sub>4</sub> nanosheets without and with addition of phosphorus dopants were labeled as G-CN and *M-Pn*-CN, respectively. Here, *M* represents the phosphorus dopant usage (weight percentage of the added phosphorus element to the dicyandiamide precursor, ranging from 0.2 to 3.2) and *Pn* (*n* = 1 or 2) meant that the corresponding dopant was H<sub>3</sub>PO<sub>4</sub> and H<sub>3</sub>PO<sub>2</sub>, respectively. Firstly, 4 g dicyandiamide and 20 g NH<sub>4</sub>Cl were premixed

with 5 mL solution containing the designed amount of dopant (for G-CN, the addition amount of dopants was zero). For example, in the preparation of 0.8-*Pn*-CN samples, the addition amounts of 85 wt% H<sub>3</sub>PO<sub>4</sub> and 50 wt% H<sub>3</sub>PO<sub>2</sub> were 119.0 and 136.3 mg, respectively. Then, the powder and solution mixture were stirred to form homogeneous slurry. Finally, the slurry was calcined with the same procedures in B-CN preparation. All the as prepared samples were collected and stored at room temperature in normal atmosphere.

Full experimental details including reagents, characterization, transient photocurrent measurement, RTK-Solar visible-light H<sub>2</sub> evolution system (Fig. S1†) and AQY measurement can be found in the ESI.†

## Results and discussion

### Morphology

Fig. 1A–D show representative g-C<sub>3</sub>N<sub>4</sub> morphologies characterized by field emission electron scanning microscope (SEM). Compared with the B-CN powder which shows a large agglomerate appearance (Fig. 1A), the g-C<sub>3</sub>N<sub>4</sub> synthesized using the NH<sub>4</sub>Cl-assisted “bottom-up” strategy shows characteristics of thin nanosheets with crinkly structures (Fig. 1B–D). It can be seen that G-CN is mainly consisted of micrometer scale petals-like nanosheets with relatively smooth surfaces and edges (Fig. 1B). The 0.8-*P1*-CN nanosheets (Fig. 1C) remain a flower-like structure and part of the nanosheets become much smaller with serrated edges, which could be ascribed to the reaction of g-C<sub>3</sub>N<sub>4</sub> nanosheets with H<sub>3</sub>PO<sub>4</sub>.<sup>18</sup> In contrast, few flower-like structures are found in the H<sub>3</sub>PO<sub>2</sub> doped powder (Fig. 1D) and even smaller nanosheets can be observed with some large nanosheets surrounded. Further to transmission electron microscope (TEM) images, the dense stacking structure of bulk B-CN is illustrated in Fig. 1E, while the as prepared g-C<sub>3</sub>N<sub>4</sub> nanosheets using NH<sub>4</sub>Cl as dynamic gas template (Fig. 1F–H) present porous structures. In the N<sub>2</sub> physisorption measurements, the specific surface areas, pore volumes and pore size distributions of the g-C<sub>3</sub>N<sub>4</sub> samples were obtained (Fig. 1I). All the tested g-C<sub>3</sub>N<sub>4</sub> samples possess well-defined mesopores. The specific areas and pore volumes of g-C<sub>3</sub>N<sub>4</sub> nanosheets are nearly 3 and 4.5 times enlarged than those of B-CN, respectively. Thus, the porous g-C<sub>3</sub>N<sub>4</sub> nanosheets assemblages appeared to us to provide more active sites for an enhanced photocatalytic performance.

### Structure characterization

In Fig. 2A we present the X-ray diffraction (XRD) patterns of the g-C<sub>3</sub>N<sub>4</sub> samples. All samples show the two characteristic diffraction peaks at around 13.0° and 27.4°, which were assigned to the in-plane (100) and interlayer-stacking (002) crystal planes of g-C<sub>3</sub>N<sub>4</sub>, respectively.<sup>2</sup> Compared with the peaks in B-CN, diffraction peaks of g-C<sub>3</sub>N<sub>4</sub> nanosheets samples (G-CN and *M-Pn*-CN) became weaker and the peak intensities of the phosphorus doped g-C<sub>3</sub>N<sub>4</sub> nanosheets were continuously weakened with increasing addition of phosphorus dopants. Notably, all H<sub>3</sub>PO<sub>2</sub> doped g-C<sub>3</sub>N<sub>4</sub> samples shows lower peak



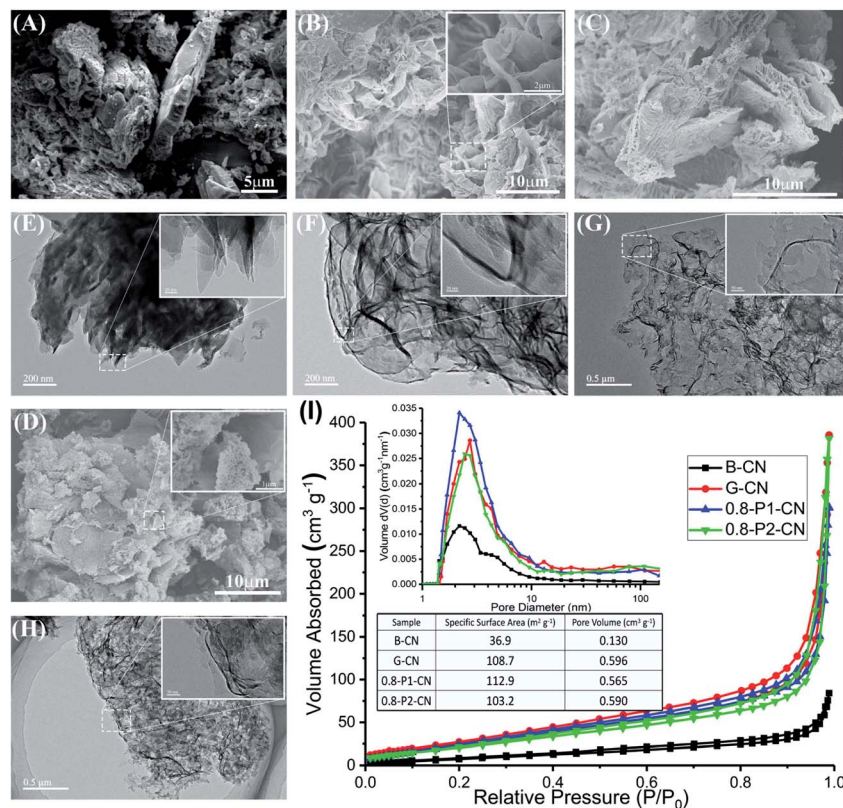


Fig. 1 (A, B, C and D) SEM images of B-CN, G-CN, 0.8-P1-CN and 0.8-P2-CN, respectively. (E, F, G and H) TEM images of B-CN, G-CN, 0.8-P1-CN and 0.8-P2-CN, respectively. (I) N<sub>2</sub> physisorption measurement results.

intensities compared to the corresponding H<sub>3</sub>PO<sub>4</sub> doped g-C<sub>3</sub>N<sub>4</sub> nanosheets at the same amount of phosphorus usage, which indicates H<sub>3</sub>PO<sub>2</sub> could more easily cause the loss of ordered structures within g-C<sub>3</sub>N<sub>4</sub> framework.<sup>2</sup> The magnified XRD patterns (inset in Fig. 2A) depict that the (002) diffraction peak of G-CN nanosheets shifted to 27.8°, suggesting a smaller gallery distance between the basic layers in the nanosheets. Earlier pioneering work<sup>6,21</sup> demonstrated that so-called planarizing the potentially undulated layers in g-C<sub>3</sub>N<sub>4</sub> would result in denser stacking, thereby resulting in shifts in the characteristic (002) diffraction peaks to higher 2θ angles. Thus, the (002) diffraction peaks shifts in XRD patterns also indicate the formation of planarized g-C<sub>3</sub>N<sub>4</sub> nanosheets as also demonstrated in our SEM studies. Interestingly, the (002) peaks of the H<sub>3</sub>PO<sub>2</sub> doped g-C<sub>3</sub>N<sub>4</sub> nanosheets continuously shifted back to around 27.5° with increasing dopant addition, while those of the H<sub>3</sub>PO<sub>4</sub> doped samples were nearly centered at the same position with G-CN (ESI, Fig. S2†). This (002) peak shift in the H<sub>3</sub>PO<sub>2</sub> doped nanosheets should be attributed to the increased disorder in the g-C<sub>3</sub>N<sub>4</sub> in-planar matrix and consequently resulted in larger layer distance compared with G-CN and H<sub>3</sub>PO<sub>4</sub> doped g-C<sub>3</sub>N<sub>4</sub> nanosheets.<sup>1,2</sup> Thus, this interesting observation suggests that this H<sub>3</sub>PO<sub>2</sub> doping protocol could help to relieve the layer stacking problems with remaining nanosheets structures.

In the Fourier Transform Infrared (FTIR) spectroscopy (Fig. 2B), the typical peaks of g-C<sub>3</sub>N<sub>4</sub> at 810 cm<sup>-1</sup> and in the

range of 900–1800 cm<sup>-1</sup> were observed among all the tested g-C<sub>3</sub>N<sub>4</sub> samples, which originated from the heptazine ring out-of-plane bending and the N–C=N heterorings in the “melon” framework.<sup>2</sup> Compared with the pristine B-CN, three distinct changes (highlighted by the orange shaded regions) occurred with varying dopants and their usages. One was the progressive loss of peak intensities in the phosphorus doped nanosheets located between 3000 and 3300 cm<sup>-1</sup> which were attributed to the N–H stretching vibrations. Another difference observed at 2184 cm<sup>-1</sup> as a new peak appeared in H<sub>3</sub>PO<sub>2</sub> doped g-C<sub>3</sub>N<sub>4</sub> nanosheets representing the stretching vibration mode of cyano groups (–C≡N).<sup>2,22,23</sup> Moreover, a weak and broad peak centered at around 3460 cm<sup>-1</sup> was developed in the g-C<sub>3</sub>N<sub>4</sub> nanosheets samples and this peak could be assigned to the stretching vibration mode of hydroxyl groups (–OH).<sup>24,25</sup> It is noteworthy that the hydroxyl group stretching vibration peaks in the H<sub>3</sub>PO<sub>2</sub> doped nanosheets are relatively stronger than those in the H<sub>3</sub>PO<sub>4</sub> doped samples, suggesting more exposure of hydroxyl groups in the H<sub>3</sub>PO<sub>2</sub> doped g-C<sub>3</sub>N<sub>4</sub> nanosheets, which will be further evidenced by the after-mentioned X-ray photoelectron spectroscopy analysis.

The FTIR results reveal that the addition of H<sub>3</sub>PO<sub>2</sub> and H<sub>3</sub>PO<sub>4</sub> in g-C<sub>3</sub>N<sub>4</sub> nanosheets synthesis could significantly decrease N–H concentration and cyano groups can be very effectively introduced by using H<sub>3</sub>PO<sub>2</sub>. The introduction of oxygen containing groups like hydroxyl group should be attributed to the high temperature (550 °C) synthesis and the



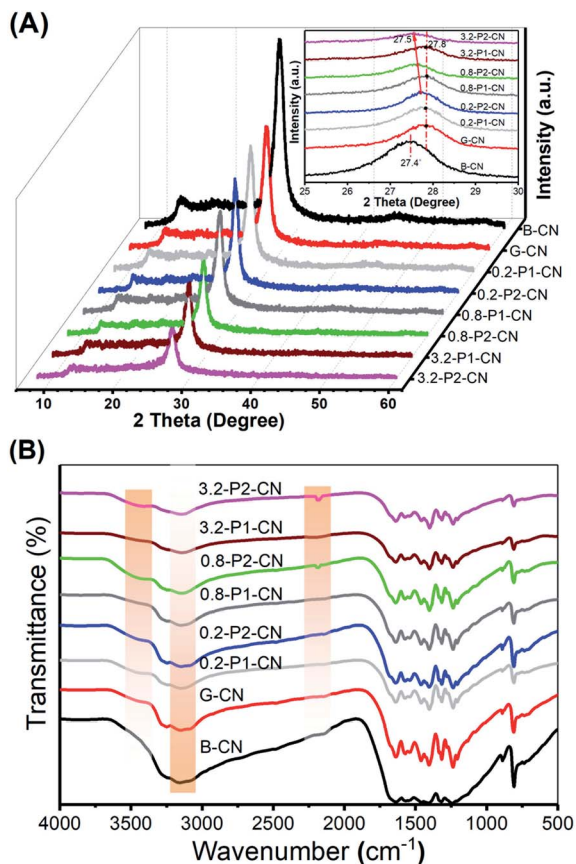


Fig. 2 (A) XRD patterns of representative  $g\text{-C}_3\text{N}_4$  samples. (B) FTIR spectra of these same samples.

atmospheric sample storage. Notably, recent research results claimed that the photocatalytic activity of  $g\text{-C}_3\text{N}_4$  can be greatly enhanced by introducing cyano groups into the melon framework.<sup>2,24</sup> Thus, the  $\text{H}_3\text{PO}_2$  doped  $g\text{-C}_3\text{N}_4$  nanosheets are expected to possess superior photocatalytic activities as would be demonstrated in the  $\text{H}_2$  production test.

Besides XRD and FTIR studies, the chemical structures of the  $g\text{-C}_3\text{N}_4$  samples were further characterized by solid-state  $^{13}\text{C}$ ,  $^{31}\text{P}$  and  $^1\text{H}$  magic angle spinning (MAS) NMR spectra. Fig. 3A presents the  $^{13}\text{C}$  NMR spectra, in which all samples show two strong peaks at 156.3 and 164.6 ppm corresponding to the chemical shifts of  $\text{C}_{3\text{N}}$  (1) and  $\text{C}_{2\text{N-NH}_x}$  (2) in the corrugated  $g\text{-C}_3\text{N}_4$  melon networks, respectively.<sup>26–28</sup> Compared with B-CN, the  $\text{C}_{3\text{N}}$  (1) peak in the  $g\text{-C}_3\text{N}_4$  nanosheets powders was intensified, which indicates the loss of  $\text{NH}_x$  groups, in accordance with the FTIR results. Moreover, G-CN and 0.8-P1-CN were found very similar, suggesting that the nonoxidative  $\text{H}_3\text{PO}_4$  would not strongly disintegrate the  $g\text{-C}_3\text{N}_4$  heptazine units. However, the  $\text{C}_{3\text{N}}$  (1) peak was further intensified in the 0.8-P2-CN sample and three new peaks (peak 3, 4 and 5) emerged. These new peaks with a chemical shift of 119.9, 112.3 and 208.1 ppm could be assigned to the carbon atoms in cyano groups,  $\text{sp}^2$  hybridized carbon atoms and the carbon atoms in the carbonyl group ( $\text{-C=O}$ ) containing species, respectively.<sup>2,28–30</sup>

No obvious differences are observed on the  $^{31}\text{P}$  NMR spectra (Fig. 3B) of 0.8-P2-CN and 0.8-P1-CN nanosheets. Both samples show single sharp peak centered at  $-0.49$  ppm which corresponds to the P-N coordinate bonds with phosphorus atom being connected to two adjacent pyridinic N atoms from two separated  $g\text{-C}_3\text{N}_4$  triazine units,<sup>31</sup> indicating that the phosphorus atoms sourced from  $\text{H}_3\text{PO}_2$  and  $\text{H}_3\text{PO}_4$  were in the same final state and interstitially doped in the  $g\text{-C}_3\text{N}_4$  matrices.<sup>32</sup> As the synthesis was conducted in the high temperature air, these doped phosphorus atoms would most likely be in pentavalent oxidation state and absorb moisture from air and eventually transform into the form of phosphoric acid. In terms of the reasons for the differences between the  $\text{H}_3\text{PO}_4$  and  $\text{H}_3\text{PO}_2$  doped  $g\text{-C}_3\text{N}_4$  nanosheets, a detailed discussion will be presented later.

Considering  $\text{NH}_4\text{Cl}$  and  $\text{H}_3\text{PO}_2$  would generate  $\text{HCl}$  and  $\text{H}_3\text{PO}_4$  which were commonly used for  $g\text{-C}_3\text{N}_4$  protonation,<sup>14,18</sup> the as prepared  $g\text{-C}_3\text{N}_4$  could be protonated. As seen in Fig. 3C, the five peaks at 2.2, 5.1, 8.7, 11.5 and 13.5 ppm in the  $^1\text{H}$  NMR spectra were assigned to the protons in aliphatic groups, residual water,  $\text{NH}_x$  groups, the hydrogen bonds in acid groups (such as carboxylic acid and phosphoric acid) and  $g\text{-C}_3\text{N}_4$  framework,<sup>33–35</sup> respectively. Thus, the intensification of the 8.7 or 11.5 ppm peak can be regarded as evidence for the protonation of  $g\text{-C}_3\text{N}_4$  nanosheets. Compared with B-CN, the 8.7 ppm peak in G-CN was obviously strengthened because of the formation of hydrogen bonds between the proton and nitrogen atoms in the  $g\text{-C}_3\text{N}_4$  framework. Despite of the weakened peaks at 8.7 ppm over the phosphorus doped nanosheets, the intensified peaks at 11.5 ppm in 0.8-P1-CN and 0.8-P2-CN should be attributed to the protonation with protons connected with phosphoric acid groups.

The measured zeta potentials (ESI, Fig. S3†) reveal that the surface charge properties were significantly changed in the  $g\text{-C}_3\text{N}_4$  nanosheets. The zeta potentials of G-CN, 0.8-P1-CN and 0.8-P2-CN were increased from  $-16.3$  mV (B-CN) to  $-6.1$ ,  $-3.1$  and  $-4.5$  mV, respectively, and these zeta potential changes further confirm the protonation of the  $g\text{-C}_3\text{N}_4$  nanosheets.<sup>15</sup> Besides the positive potential on the dispersibility, electronic bandgap structure and surface area of  $g\text{-C}_3\text{N}_4$ , one of the other important advantages of protonation is to induce higher ionic conductivity to the  $g\text{-C}_3\text{N}_4$  framework and then enable the acceleration of charge carrier migration, which would benefit for better photocatalytic performances.<sup>14,18,36</sup> Thus, higher  $\text{H}_2$  evolution ability could be expected for the protonated  $g\text{-C}_3\text{N}_4$  nanosheets.

In addition, combining with the newly emerged carbonyl group peak in the  $^{13}\text{C}$  spectra and the enhanced acid groups hydrogen bonds  $^1\text{H}$  NMR signal in 0.8-P2-CN nanosheets, it is reasonable to propose that carboxyl groups ( $\text{-COOH}$ ) were introduced into the  $\text{H}_3\text{PO}_2$  doped nanosheets, thereby resulting in a stronger 11.5 ppm peak in 0.8-P2-CN than that of 0.8-P1-CN, and this peak intensification is in agreement with the observation that the  $\text{H}_3\text{PO}_2$  doped  $g\text{-C}_3\text{N}_4$  nanosheets showed stronger hydroxyl group ( $\text{-OH}$ ) peak intensities in FTIR spectra.



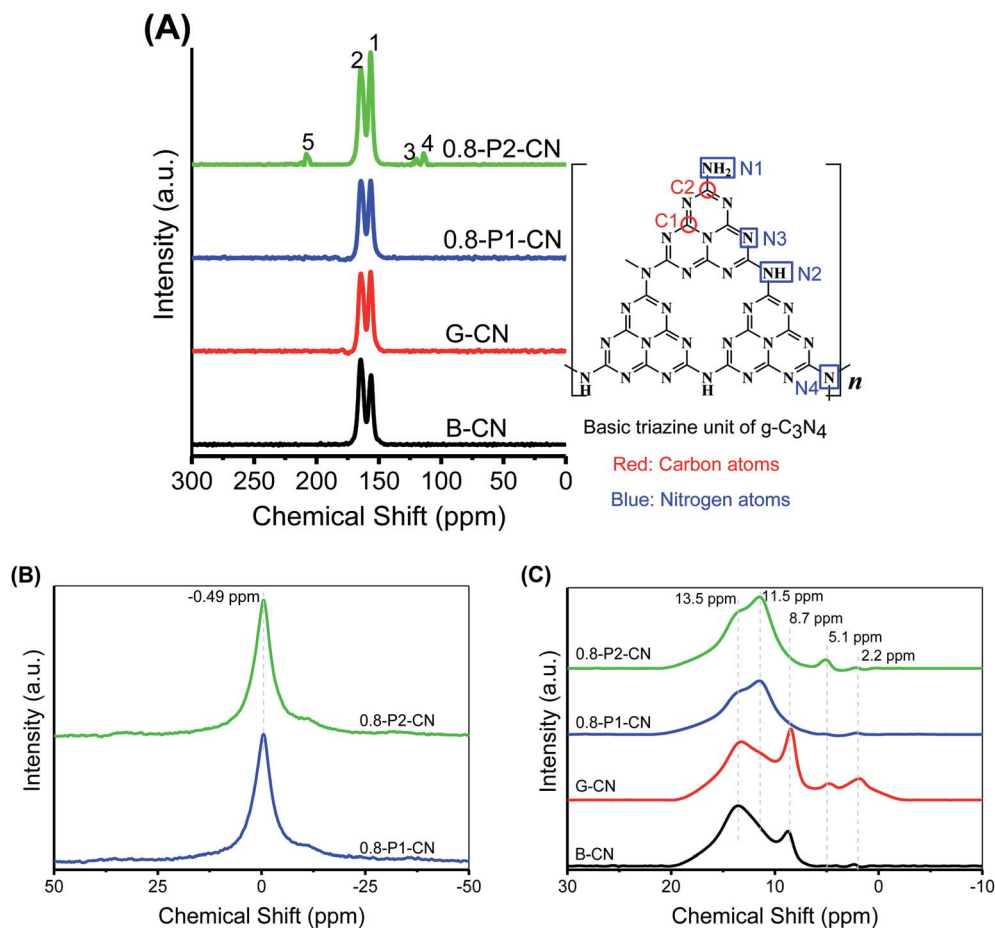


Fig. 3 (A) Solid-state NMR spectra of  $^{13}\text{C}$  and basic  $\text{g-C}_3\text{N}_4$  triazine unit structure. (B and C) Solid-state  $^{31}\text{P}$  and  $^1\text{H}$  NMR spectrums, respectively.

### Chemical compositions

The  $\text{g-C}_3\text{N}_4$  compositions obtained from organic elemental analysis (OEA) and X-ray photoelectron spectroscopy (XPS) can be found in Table 1 (ESI, XPS spectra in Fig. S4<sup>†</sup>). As can be seen in Table 1, the increased H/C ratios in  $\text{g-C}_3\text{N}_4$  nanosheets can also be regarded as evidences for protonation.<sup>15</sup> The N/C atomic ratio of B-CN obtained from OEA and XPS were 1.467 and 1.318, respectively. According to XPS results, the N/C ratio of G-CN

Table 1 Element atomic ratios of the  $\text{g-C}_3\text{N}_4$  samples<sup>a</sup>

Sample	OEA			XPS		
	N/C	O/C	H/C	N/C	O/C	P/C
B-CN	1.467	0.007	0.023	1.318	0.038	0
G-CN	1.421	0.018	0.027	1.283	0.064	0
0.2-P1-CN	1.389	0.047	0.029	1.287	0.079	0.018
0.8-P1-CN	1.381	0.064	0.031	1.266	0.105	0.038
3.2-P1-CN	1.365	0.073	0.032	1.249	0.112	0.043
0.2-P2-CN	1.293	0.091	0.030	1.204	0.127	0.010
0.8-P2-CN	1.117	0.135	0.035	1.037	0.223	0.017
3.2-P2-CN	1.002	0.162	0.037	0.904	0.279	0.024

<sup>a</sup> OEA and XPS represent the results obtained from organic elemental analysis and X-ray photoelectron spectroscopy, respectively.

slightly decreased from 1.318 to 1.283 when B-CN was transformed into G-CN, and this was ascribed to higher degree polymerization with more  $\text{NH}_3$  release during the formation of nanosheet structures.<sup>7</sup> Although the N/C ratio of  $\text{H}_3\text{PO}_4$  doped nanosheets dropped to about 1.249, it was still very close to that of G-CN. However, the N/C ratio of  $\text{H}_3\text{PO}_2$  doped  $\text{g-C}_3\text{N}_4$  nanosheets fell to 0.904 as a result of the intensive loss of nitrogen caused by the addition of  $\text{H}_3\text{PO}_2$ . Meanwhile, the O/C ratio of the  $\text{H}_3\text{PO}_2$  doped  $\text{g-C}_3\text{N}_4$  nanosheets drastically increased to 0.279. Thus, it was most likely that the  $\text{H}_3\text{PO}_2$  induced the opening of  $\text{g-C}_3\text{N}_4$  heptazine rings and caused nitrogen vacancies. The exposed defective edges would then react with oxygen to form oxygen containing groups such as carboxyl groups *etc.*<sup>24</sup>

In accordance with the fact that  $\text{H}_3\text{PO}_2$  will decompose to release both  $\text{PH}_3$  and  $\text{H}_3\text{PO}_4$ ,<sup>4</sup> the differences highlighted between the  $\text{H}_3\text{PO}_2$  and  $\text{H}_3\text{PO}_4$  doped  $\text{g-C}_3\text{N}_4$  nanosheets provides strong evidence that the introduction of nitrogen vacancies can be attributed to the strongly reductive  $\text{PH}_3$  rather than  $\text{H}_3\text{PO}_4$ . In the reduction synthesis of nitrogen defective  $\text{g-C}_3\text{N}_4$ ,<sup>16</sup> the energy changes for removing a lattice nitrogen atom located at N1, N2, N3 and N4 (referring to Fig. 3A) and terminating the dangling bonds of C atoms with H atoms using  $\text{H}_2$  as reduction agent were 0.65, 0.83, 1.40 and 2.39 eV, respectively,<sup>16</sup> and the  $\text{H}_2$  reduction caused homogeneous  $\text{sp}^2$  hybridized



nitrogen atoms losses on the  $g\text{-C}_3\text{N}_4$  heptazine rings. Changing  $\text{H}_2$  to  $\text{PH}_3$ , we calculated the corresponding energy changes and the four energy changes decrease to 0.61, 0.75, 1.28 and 2.27 eV ( $\text{ESI}^\dagger$ ), respectively, indicating the stronger reduction agent  $\text{PH}_3$  would be more favorable for opening heptazine rings and result in significant nitrogen atoms *in situ* reduction removal. Thus, it was reasonable to propose that intensive nitrogen vacancies could be introduced into the  $\text{H}_3\text{PO}_2$  doped  $g\text{-C}_3\text{N}_4$  nanosheets because of that the strong reducing agent  $\text{PH}_3$ , produced *via*  $\text{H}_3\text{PO}_2$  decomposition.

The narrow scan C 1s, N 1s, P 2p and O 1s XPS spectra were collected and deconvoluted into their components (Fig. 4A–D). The four peaks in C 1s spectra are located at 284.8, 286.2, 288.1 and 289 eV, corresponding to the adventitious hydrocarbons (C–C or C=C), C– $\text{NH}_x$  ( $x = 1, 2$ ), N–C=N coordination and carboxyl groups, respectively.<sup>2,37,38</sup> It is obvious that the 288.1 eV signal lost intensity, while the 286.2 eV peak is significantly intensified in the 0.8-P2-CN powder. As cyano group has similar C 1s binding energy to C– $\text{NH}_x$ ,<sup>2</sup> the intensified 286.2 eV signal together with the weakened N–C=N coordination peak could be further evidence for the heptazine rings opening and the formation of cyano groups in the  $\text{H}_3\text{PO}_2$  doped nanosheets. Besides, the enhanced 289 eV peak in 0.8-P2-CN confirms the considerable introduction of carboxyl groups into  $\text{H}_3\text{PO}_2$  doped  $g\text{-C}_3\text{N}_4$  nanosheets. The three peaks centered at 398.6, 400 and 401 eV in the N 1s XPS spectra are assigned to the  $\text{sp}^2$ -hybridized ( $\text{N}_{2\text{C}}$ ),  $\text{sp}^3$ -hybridized

( $\text{N}_{3\text{C}}$ ) nitrogen atoms and  $\text{NH}_x$  groups, respectively.<sup>2</sup> For the  $\text{H}_3\text{PO}_2$  doped nanosheets, the drastically weakened  $\text{NH}_x$  peak and shift of  $\text{N}_{3\text{C}}$  to lower binding energy also indicate the  $\text{NH}_x$  loss and formation of cyano groups, which are in agreement with the results obtained by FTIR and NMR spectra.

Both the P 2p XPS spectra of the  $\text{H}_3\text{PO}_4$  and  $\text{H}_3\text{PO}_2$  doped nanosheets show one single pentavalent phosphorus peak centered at 133.8 eV, indicating that no P–C bonds formed.<sup>18</sup> Moreover, the elemental mapping conducted on scanning transmission microscope ( $\text{ESI}$ , Fig. S5 $^\dagger$ ) reveal that phosphorus is distributed evenly in both 0.8-P1-CN and 0.8-P2-CN with an actual content of around 0.5 wt%. The parallel intensification of the 533.5 and 532.2 eV peaks representing –OH and C=O groups<sup>39–41</sup> in the 0.8-P2-CN O 1s spectra are consistent with the hypothesis that carboxyl groups was introduced into the  $\text{H}_3\text{PO}_2$  doped  $g\text{-C}_3\text{N}_4$  nanosheets. According to the summarized XPS data ( $\text{ESI}$ , Table S1 $^\dagger$ ), the  $\text{N}_{2\text{C}}/\text{C}$  ratio in the  $g\text{-C}_3\text{N}_4$  nanosheets remarkably dropped from 0.917 to 0.568 and the corresponding O/C ratio increased from 0.062 to 0.217 with the addition of  $\text{H}_3\text{PO}_2$ , these results also suggest the introduction of nitrogen defects and oxygen species into the  $\text{H}_3\text{PO}_2$  doped  $g\text{-C}_3\text{N}_4$  nanosheets.

### Proposed schematic structures

Further to our XPS and OEA analysis, electron paramagnetic resonance (EPR) experiments were conducted to provide fingerprint evidence for probing the surface nitrogen vacancies

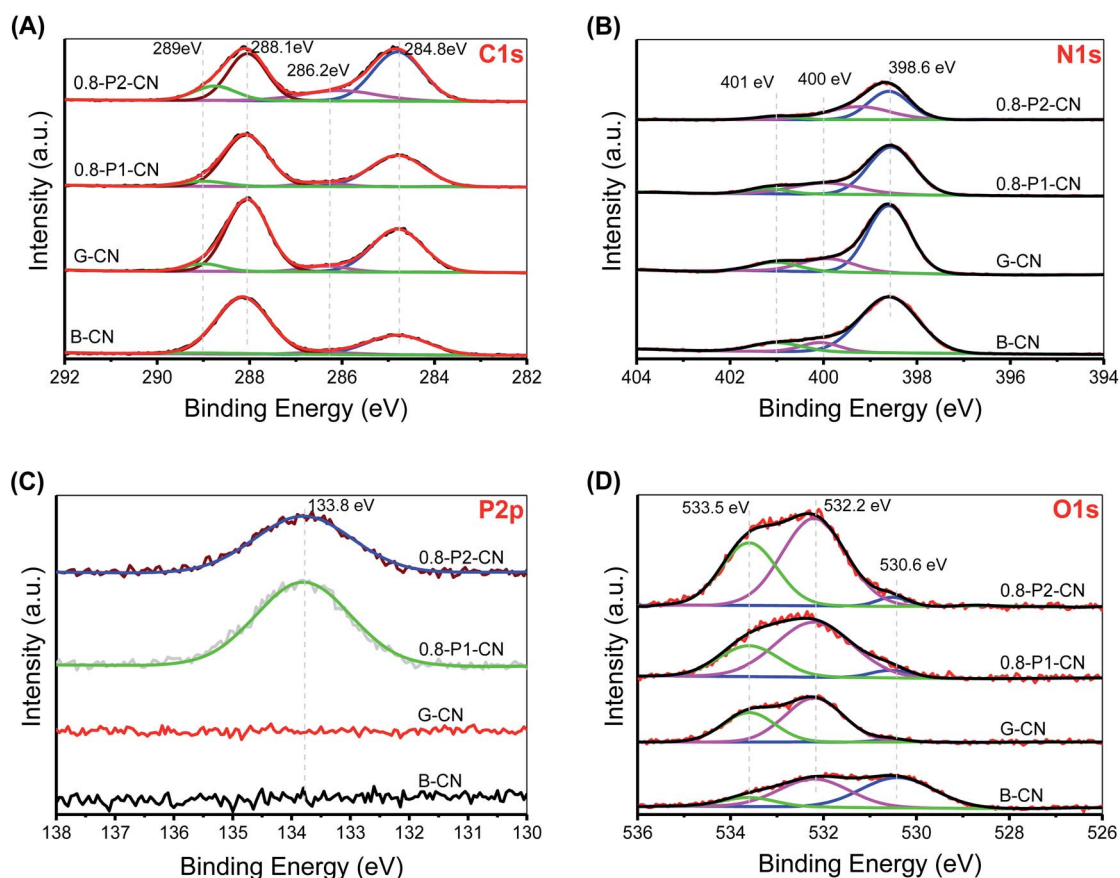


Fig. 4 (A) C 1s XPS narrow scan. (B) N 1s XPS narrow scan. (C) P 2p XPS narrow scan. (D) O 1s XPS narrow scan.



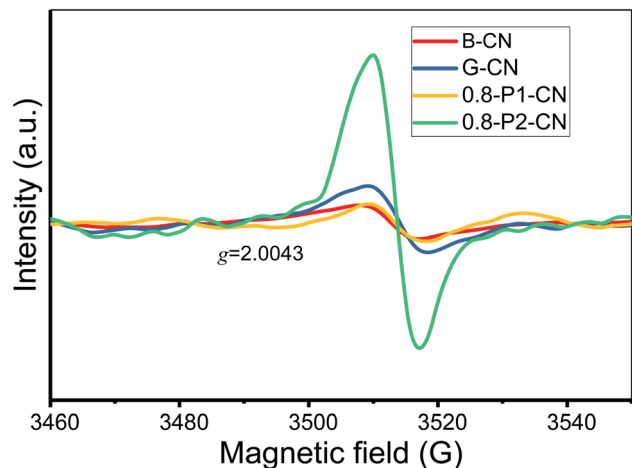


Fig. 5 EPR spectra of the representative  $g\text{-C}_3\text{N}_4$  samples.

introduced to the  $g\text{-C}_3\text{N}_4$  nanosheets. Several different samples having closely similar weights were examined to ensure a meaningful comparison of the peak intensities (areas). As shown in Fig. 5, all samples display a single Lorentzian line with an electronic  $g$  value of 2.0043 in the magnetic field from 3460 to 3560 G, which represents the unpaired electrons of  $sp^2$  hybrid carbon atoms in  $\pi$ -conjugated aromatic rings.<sup>42,43</sup> Thus the formation of two-coordinated nitrogen vacancies in the heptazine rings of  $g\text{-C}_3\text{N}_4$  would donate unpaired electrons to the  $sp^2$ -

carbon atoms. Therefore, compared with the negligible EPR signals of B-CN, G-CN and 0.8-P1-CN, the significantly enhanced EPR intensity in 0.8-P2-CN nanosheets adds weight to the idea of the opening of heptazine rings and the formation of two-coordinated nitrogen vacancies.

Thus, we believe that combining the various techniques including FTIR, NMR, zeta potential, XPS and EPR analysis, the controllable generation of nitrogen vacancies, protonation and newly introduced functional groups in  $g\text{-C}_3\text{N}_4$  framework are soundly confirmed. From all this information, the proposed schematic molecule structures and evolution processes of the  $g\text{-C}_3\text{N}_4$  samples can now be advanced (Fig. 6).

In brief, compared with the directly polymerized bulk  $g\text{-C}_3\text{N}_4$  agglomerate, protonated  $g\text{-C}_3\text{N}_4$  nanosheets could be readily fabricated with the help of dynamic gas template  $\text{NH}_4\text{Cl}$ . With co-addition of  $\text{H}_3\text{PO}_4$  as dopant, the  $g\text{-C}_3\text{N}_4$  nanosheets could be further protonated with phosphorus atoms interstitially doped into the frameworks. However, apart from the additional protonation, the addition of the reducing dopant  $\text{H}_3\text{PO}_2$  could also induce significant nitrogen loss to generate nitrogen vacancies and variously introduce, cyano and carboxyl functional groups, into the  $g\text{-C}_3\text{N}_4$  nanosheets.

### Optical properties

The optical properties and light harvesting abilities of  $g\text{-C}_3\text{N}_4$  samples were significantly modified by the specific addition of  $\text{NH}_4\text{Cl}$  and phosphorus dopants. The obvious changes were well

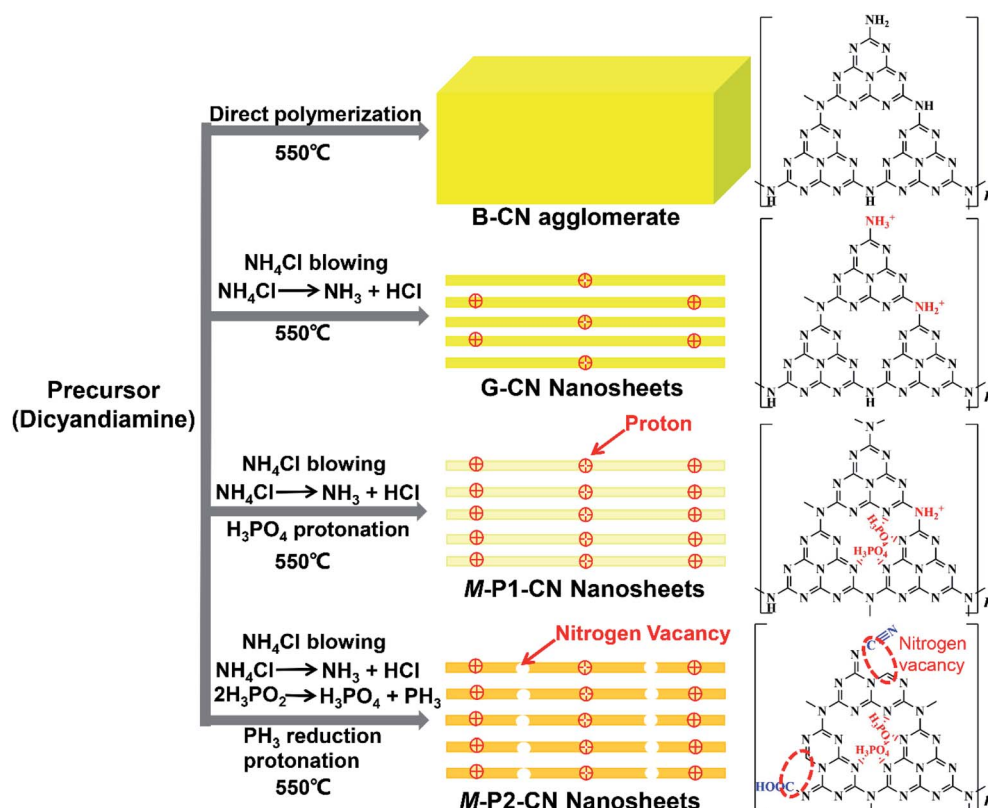


Fig. 6 The  $g\text{-C}_3\text{N}_4$  evolution process and proposed chemical structures.



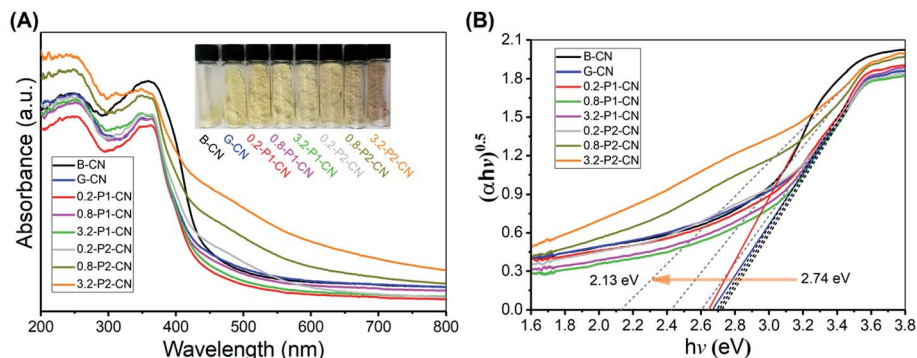


Fig. 7 (A) UV-Vis DRS spectra and. (B) Plots of transformed Kubelka–Munk function versus photon energy for a variety of g-C<sub>3</sub>N<sub>4</sub> samples.

observed as the yellow dense B-CN powder was transformed into porous and fluffy states having different colours (Fig. 7A). Compared with B-CN and G-CN, the colours of the M-P1-CN nanosheets became lighter with the increasing addition of H<sub>3</sub>PO<sub>4</sub>, whereas those of the H<sub>3</sub>PO<sub>2</sub> doped nanosheets turned from dark yellow to brown. The absorption edge of G-CN shifted to a lower wavelength as compared with B-CN and it

continuously shifted to the lower direction with increasing H<sub>3</sub>PO<sub>4</sub> addition. The blueshifts in the G-CN and H<sub>3</sub>PO<sub>4</sub> doped nanosheets were attributed to the enhanced protonation.<sup>5,14</sup> Unlike H<sub>3</sub>PO<sub>4</sub>, a progressive redshift was achieved by increasing H<sub>3</sub>PO<sub>2</sub> usage, which indicates the bandgap structures of the H<sub>3</sub>PO<sub>2</sub> doped nanosheets could be easily tuned by adjusting the amount of H<sub>3</sub>PO<sub>2</sub>.

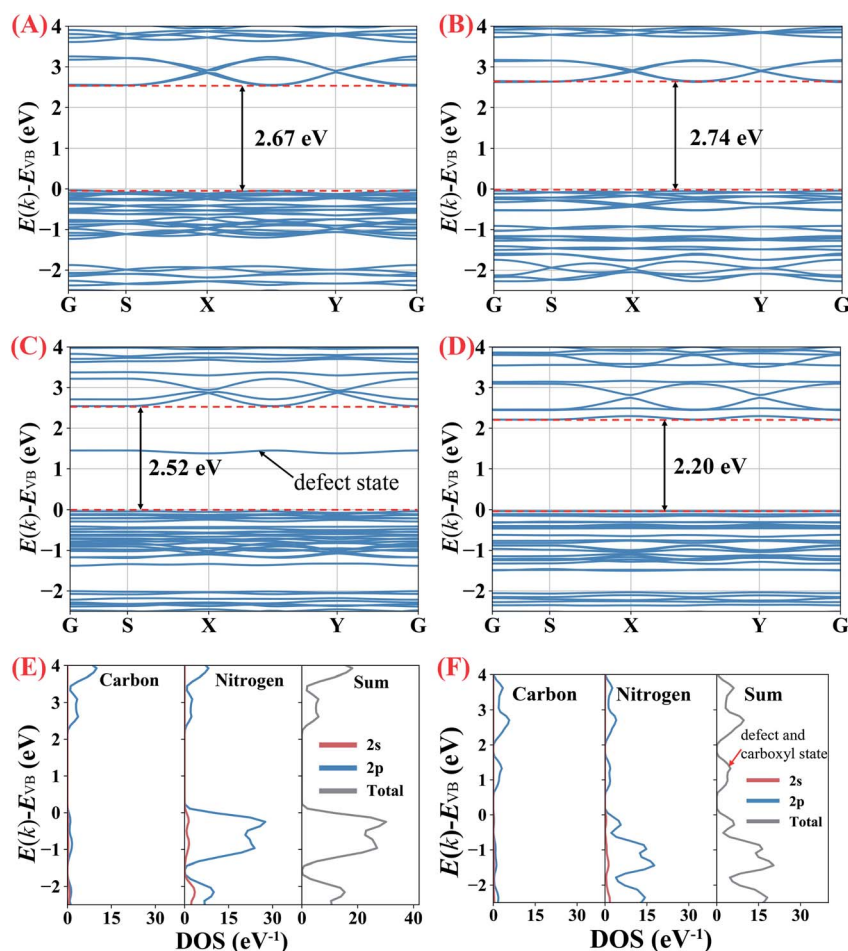


Fig. 8 (A–D) Calculated band structures of B-CN and g-C<sub>3</sub>N<sub>4</sub> with protonation, nitrogen vacancies and carboxyl groups, respectively. (E and F) corresponding PDOS for B-CN and g-C<sub>3</sub>N<sub>4</sub> containing nitrogen vacancies and carboxyl groups, respectively.



According to the transformed Kubelka–Munk function determined electronic bandgaps shown in Fig. 7B, the bandgaps of  $\text{H}_3\text{PO}_4$  doped  $\text{g-C}_3\text{N}_4$  nanosheets were slightly increased to a narrow range of 2.70–2.74 eV from 2.67 eV (G-CN), while that of the  $\text{H}_3\text{PO}_2$  doped nanosheets can be significantly narrowed to 2.13 eV. The narrowed bandgaps reveal the enhanced visible light harvesting ability of the nitrogen deficient  $\text{g-C}_3\text{N}_4$  nanosheets which were doped by  $\text{H}_3\text{PO}_2$ .

To understand the influence of protonation (including both the protons which connect with nitrogen atoms and the interstitially doped phosphoric acid groups), nitrogen vacancies and carboxyl groups ( $-\text{COOH}$ ) on the bandgaps of the  $\text{g-C}_3\text{N}_4$  samples, partial density of states (PDOS) and density-functional theory (DFT) calculations were performed (ESI for details, Fig. S6†).

As shown in Fig. 8A and B, the calculated bandgap for B-CN is 2.67 eV which becomes slightly enhanced to 2.74 eV in the protonated  $\text{g-C}_3\text{N}_4$  nanosheets, indicating that the protonation (no matter induced by  $\text{NH}_4\text{Cl}$  gas template or interstitially doped phosphorus) does not significantly impact on the magnitude of bandgap. To clarify the effects of the nitrogen vacancies and carboxyl groups,  $\text{g-C}_3\text{N}_4$  unit cells only containing

nitrogen vacancies or carboxyl groups were built, respectively. The calculations in Fig. 8C and D show that the nitrogen vacancies and the carboxyl groups decrease the bandgap to 2.52 and 2.20 eV, respectively. The defect energy level observed in the  $\text{g-C}_3\text{N}_4$  only containing nitrogen vacancies, composing of both C 2p and N 2p orbitals, is about 1.5 eV above valence band (VB). The narrowed bandgap of the  $\text{g-C}_3\text{N}_4$  containing nitrogen vacancies and carboxyl groups agrees with the trend observed in the UV-Vis DRS analysis above. As the PDOS seen in Fig. 8E, the conduction band (CB) of B-CN is composed of C 2p and N 2p orbits, while C 2p and N 2p orbits mainly contribute to valence band; this result is consistent with previous work.<sup>2,44</sup> According to Fig. 8F, the significantly narrowed bandgap width of the  $\text{H}_3\text{PO}_2$  doped  $\text{g-C}_3\text{N}_4$  nanosheets is due primarily to a lowering of CB minimum by about 0.4 eV with the emergence of defect and carboxyl states. These results therefor confirm that the coexistence of nitrogen vacancies and carboxyl groups would decrease the width of  $\text{g-C}_3\text{N}_4$  bandgap. As confirmed in previous work,<sup>2</sup> the coexistence of cyano groups and nitrogen vacancies would also lower the CB minimum and result in narrower electronic energy bandgaps. By analogy, the coexistence of

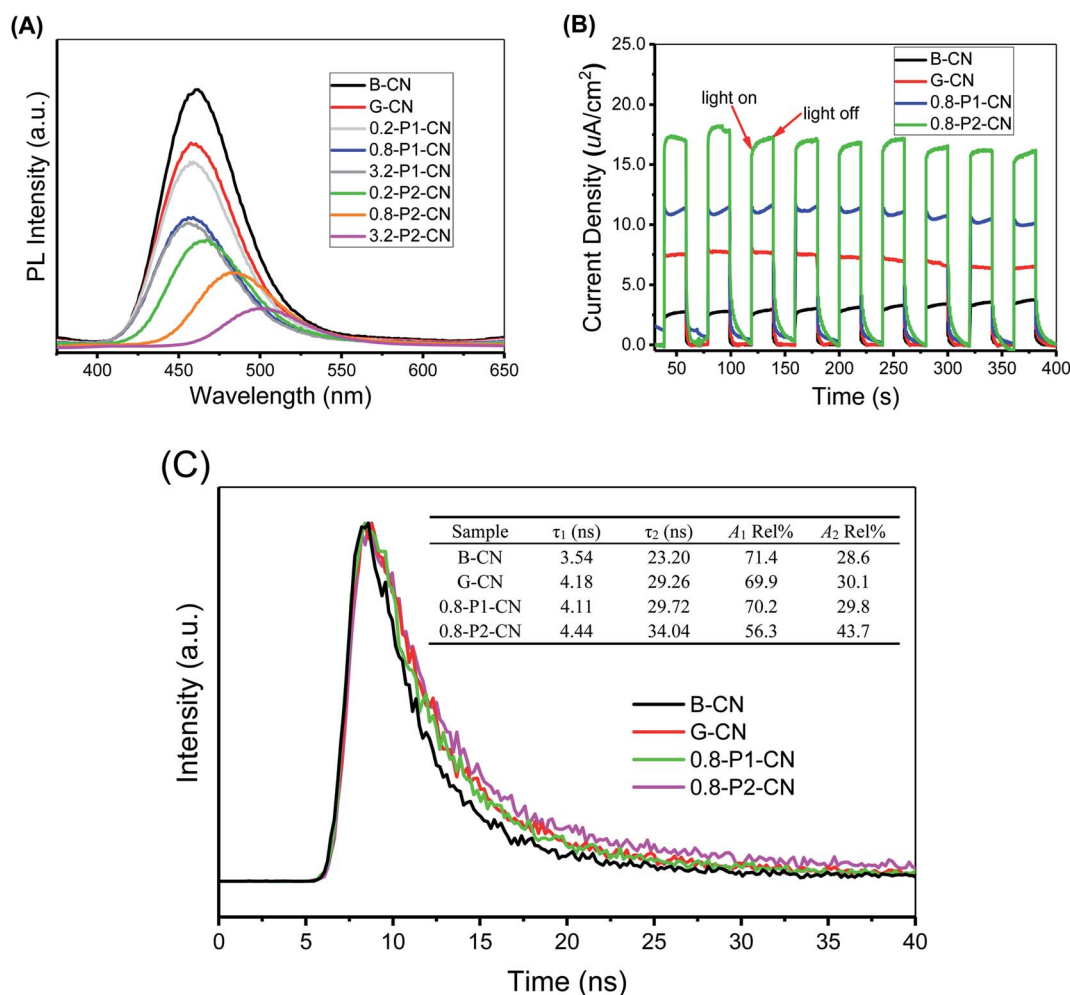


Fig. 9 (A) Photoluminescence (PL) spectra and (B) photocurrent curves for B-CN and representative  $\text{g-C}_3\text{N}_4$  nanosheet materials. (C) Time-resolved photoluminescence decay spectra for representative  $\text{g-C}_3\text{N}_4$  samples.



cyano groups, carboxyl groups and nitrogen vacancies would synergistically decrease the bandgap width of the as prepared  $g\text{-C}_3\text{N}_4$  nanosheets which were doped by  $\text{H}_3\text{PO}_2$ .

As the photoluminescence (PL) spectra illustrated in Fig. 9A, B-CN shows an intense fluorescence signal at around 460 nm under visible-light irradiation and this signal in G-CN is significantly decreased. Because the PL spectra can be interpreted as the radiative recombination of surface trapping states, thus the weakened PL intensity could indicate the enhanced separation of photo-excited electrons and holes.<sup>45,46</sup> By adding  $\text{H}_3\text{PO}_4$ , the peak is further weakened. It is noted that much lower peak intensities are found over  $\text{H}_3\text{PO}_2$  doped  $g\text{-C}_3\text{N}_4$  nanosheets and the peak continuously shifts to around 510 nm with the increasing addition of  $\text{H}_3\text{PO}_2$ . The PL peak red-shift in the  $\text{H}_3\text{PO}_2$  doped  $g\text{-C}_3\text{N}_4$  nanosheets is associated with the decreased bandgap energy of the samples and consistent with the trend as seen in UV-Vis DRS.<sup>46</sup> As illustrated in Fig. 9B, all samples exhibit sensitive photocurrent responses during the visible-light on/off irradiation. The photocurrent density values for the four representative samples (B-CN, G-CN, 0.8-P1-CN and 0.8-P2-CN) are  $\approx 2.5$ , 7.5, 11.1 and  $17.0 \mu\text{A cm}^{-2}$ , respectively.

To investigate the dynamic electron immigration process, time-resolved fluorescence spectra were collected. As seen in Fig. 9C, the lifetime of the photo-induced charge carriers in the  $\text{H}_3\text{PO}_2$  doped  $g\text{-C}_3\text{N}_4$  nanosheets were significantly prolonged compared with B-CN, G-CN and  $\text{H}_3\text{PO}_4$  doped nanosheets sample, revealing the accelerated charge transfer performance.<sup>46</sup>

Both photoluminescence and photocurrent tests indicate that the  $g\text{-C}_3\text{N}_4$  nanosheets possess much better performance in the critical process of photo-excited charge carrier separation and visible-light response than the corresponding directly polymerized B-CN. Regarding G-CN and  $\text{H}_3\text{PO}_4$  doped  $g\text{-C}_3\text{N}_4$  nanosheets, the enhanced separation of charge carriers could be attributed to their large specific surface areas and protonation.<sup>7,14</sup> Besides, the interstitially doped phosphorus atoms in the  $\text{H}_3\text{PO}_4$  doped  $g\text{-C}_3\text{N}_4$  nanosheets would likely facilitate optimization of the  $\pi$ -conjugated heptazine rings to improve the carrier mobility and offer a new channel for carrier migration,<sup>18,32</sup> thereby offering enhanced charge carriers separation. Besides the interstitial phosphorus doping, the nitrogen vacancies in the  $\text{H}_3\text{PO}_2$  doped  $g\text{-C}_3\text{N}_4$  nanosheets would also induce unpaired  $sp^2$ -carbon atoms within the  $\pi$ -conjugated heptazine rings. These electron defected  $sp^2$ -carbon atoms and newly introduced electron-withdrawing groups (cyano and carboxyl groups) can redistribute the  $\pi$ -electrons and result in improved visible light absorption and photo-excited charge carriers separation.<sup>4,47–49</sup> Thus, a confluence of the synergistic effect of protonation, interstitial phosphorus doping, nitrogen vacancies and newly introduced functional groups in the  $\text{H}_3\text{PO}_2$  doped  $g\text{-C}_3\text{N}_4$  nanosheets was achieved and expected to offer a comprehensive enhancement of visible-light photocatalysis. We now turn to these experiments.

### Photocatalytic $\text{H}_2$ evolution performances

The photocatalytic performances of the  $g\text{-C}_3\text{N}_4$  samples were evaluated by measuring the visible-light ( $\lambda \geq 400 \text{ nm}$ )  $\text{H}_2$

evolution in 20 vol% triethanolamine (TEOA) aqueous solution with 1.5 wt% of Pt loading. As shown in Fig. 10A, the  $g\text{-C}_3\text{N}_4$  nanosheets exhibited much higher photocatalytic activities than the standard reference B-CN. The  $\text{H}_2$  generation rate of G-CN reached  $99.1 \mu\text{mol h}^{-1}$ , whilst only  $41.6 \mu\text{mol h}^{-1}$  was obtained over B-CN. Importantly, the  $\text{H}_2$  evolution rate of  $g\text{-C}_3\text{N}_4$  nanosheets was significantly improved with the doping of  $\text{H}_3\text{PO}_4$  and  $\text{H}_3\text{PO}_2$ , respectively. The  $\text{H}_3\text{PO}_4$  doped  $g\text{-C}_3\text{N}_4$  nanosheets exhibited a  $\text{H}_2$  evolution rate of  $144.2 \mu\text{mol h}^{-1}$  by the 1.6-P1-CN sample. Interestingly, 0.8-P1-CN and 3.2-P1-CN gave a very similar  $\text{H}_2$  evolution rate as 1.6-P1-CN, which could be ascribed to that the limited visible light absorption of the  $\text{H}_3\text{PO}_4$  protonated  $g\text{-C}_3\text{N}_4$  nanosheets confines the highest  $\text{H}_2$  evolution rate when a certain level of  $\text{H}_3\text{PO}_4$  addition was reached. For the  $\text{H}_3\text{PO}_2$  doped nanosheets, 0.8-P2-CN showed the highest  $\text{H}_2$  evolution rate of  $255.3 \mu\text{mol h}^{-1}$  which was 6.14,

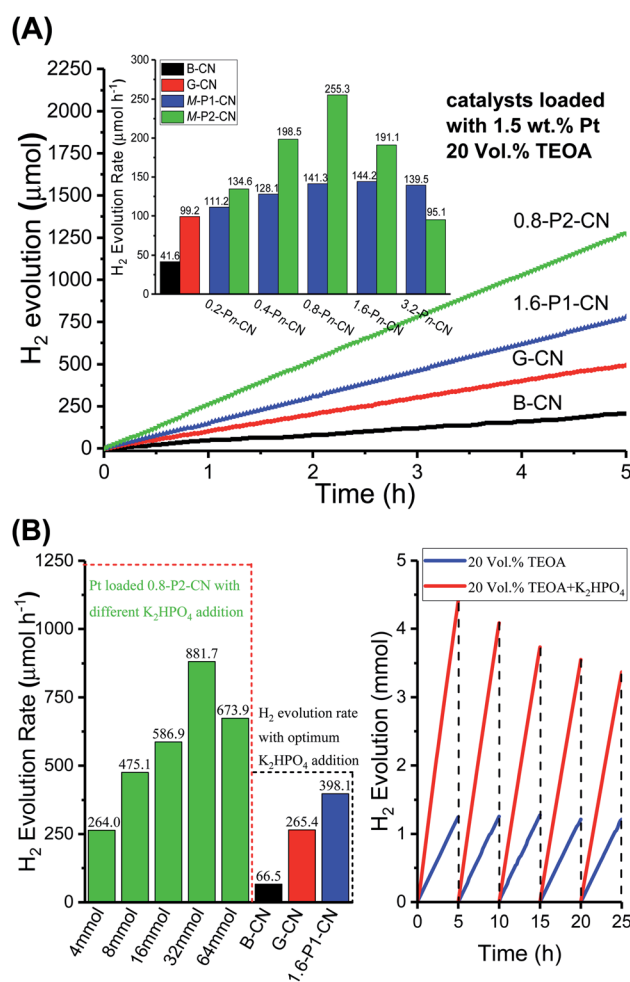


Fig. 10 (A) Rates and time-on-stream of the photocatalytic  $\text{H}_2$  evolution over 1.5 wt% Pt-loaded  $g\text{-C}_3\text{N}_4$  samples in 20 vol% TEOA solution under visible-light irradiation ( $\lambda \geq 400 \text{ nm}$ ). The  $g\text{-C}_3\text{N}_4$  usage in each experiment was 15 mg. (B)  $\text{H}_2$  evolution rates over the 1.5 wt% Pt-loaded B-CN, G-CN, 1.6-P1-CN and 0.8-P2-CN in the 20 vol% TEOA solution with optimum addition of  $\text{K}_2\text{HPO}_4$  (left). Time course of the long-term  $\text{H}_2$  evolution over the 0.8-P2-CN nanosheets loaded with 1.5 wt% Pt in 20 vol% TEOA and the optimum TEOA/ $\text{K}_2\text{HPO}_4$  mixture solution (right).



2.58 and 1.77 times of that over B-CN, G-CN and 1.6-P1-CN, respectively. The bandgap structures determined by the valence band XPS spectra and UV-Vis DRS results indicate that the narrowed bandgap of the  $\text{H}_3\text{PO}_2$  doped  $\text{g-C}_3\text{N}_4$  nanosheets originates from the conduction band decrease (ESI, Fig. S7 and Table S2†). Thus, the excessively lowered reduction driving force for  $\text{H}_2$  evolution may result in lower  $\text{H}_2$  evolution activity even though the visible light harvesting ability of  $\text{g-C}_3\text{N}_4$  was progressively intensified by increasing  $\text{H}_3\text{PO}_2$  usage. These findings could explain why the highest  $\text{H}_2$  generation performance was achieved on the Pt loaded 0.8-P2-CN.

Because our RTK-Solar  $\text{H}_2$  evolution system was used for the first time for photocatalytic  $\text{H}_2$  evolution tests, its accuracy was verified in two steps. First, the evolved gas was confirmed to be only  $\text{H}_2$  with the help of Hiden HPR 20 gas chromatograph/mass spectrometer system (ESI, Fig. S8†). Second,  $\text{H}_2$  evolution experiments over 1.5 wt% Pt loaded B-CN, G-CN, 1.6-P1-CN and 0.8-P2-CN in 20 vol% TEOA solution were further conducted under the same conditions as those in the RTK-Solar system. With the quartz reactor being connected to a gas circulation system, the generated  $\text{H}_2$  amount was quantified by a calibrated gas chromatography equipped TCD detector (Clarus 580, PerkinElmer, helium as carrier gas) for every 1 hour. The gas chromatography determined  $\text{H}_2$  evolution rates over the 1.5 wt% Pt loaded B-CN, G-CN, 1.6-P1-CN and 0.8-P2-CN were 42.8, 106.6, 140.1 and 261.6  $\mu\text{mol h}^{-1}$ , respectively (ESI, Fig. S9 and Table S3†). The ratios of the  $\text{H}_2$  evolution rates determined by gas chromatography method and the RTK-Solar system over the four representative  $\text{g-C}_3\text{N}_4$  samples were located in a very narrow range of 0.972 to 1.076, confirming the reliability of RTK-Solar system for measuring the amount of generated  $\text{H}_2$ . The photocatalytic  $\text{H}_2$  evolution results reveal the significantly enhanced  $\text{g-C}_3\text{N}_4$  photocatalytic performance over the nitrogen deficient and protonated  $\text{g-C}_3\text{N}_4$  nanosheets produced by this facile *in situ* reductive synthesis strategy.

As proposed by Ye,<sup>1</sup> using the nature-inspired strategy of adding  $\text{K}_2\text{HPO}_4$  to TEOA solution, the  $\text{H}_2$  evolution performance of  $\text{g-C}_3\text{N}_4$  could be significantly enhanced. In Ye's important work,<sup>1</sup> it was shown that the added  $\text{HPO}_4^{2-}$  can function both as a proton-pump in natural photosynthesis (to facilitate proton transport in the reaction solution) and also act as a mediator to give rise to a new proton-reduction pathway. The use of  $\text{HPO}_4^{2-}$  instead of  $\text{H}_2\text{O}$  provides the necessary protons to react with photo-generated electrons to produce  $\text{H}_2$  and  $\text{PO}_4^{3-}$  on the surface of Pt co-catalyst at the very beginning. Following the  $\text{H}_2$  evolution from  $\text{HPO}_4^{2-}$ , the resulting  $\text{PO}_4^{3-}$  entity immediately combined with  $\text{H}^+$  from  $\text{H}_2\text{O}$  to regenerate  $\text{HPO}_4^{2-}$  and finally complete the proton-reduction cycle.

In other words, the added  $\text{K}_2\text{HPO}_4$  would not be consumed during the photocatalytic  $\text{H}_2$  evolution. In addition,  $\text{K}_2\text{HPO}_4$  would also promote the oxidation of TEOA. The synergy of enhanced proton reduction and improved photooxidation of TEOA boosted the visible-light photocatalytic  $\text{H}_2$  evolution over the Pt loaded  $\text{g-C}_3\text{N}_4$  catalysts. Thus, enhanced  $\text{H}_2$  evolution over the Pt loaded 0.8-P2-CN could also be expected by adding  $\text{K}_2\text{HPO}_4$  to the TEOA solution.

As illustrated in Fig. 10B, with the optimum addition of  $\text{K}_2\text{HPO}_4$  (32 mmol) to the 20 vol% TEOA solution, the  $\text{H}_2$  evolution of the Pt loaded 0.8-P2-CN was drastically enhanced to a rate of 881.7  $\mu\text{mol h}^{-1}$ , and impressive  $\text{H}_2$  generation could be observed (ESI, Video S1†). Similarly, the  $\text{H}_2$  generation rates of the Pt loaded B-CN, G-CN and 1.6-P1-CN were also promoted by the optimum TEOA/ $\text{K}_2\text{HPO}_4$  solution, but the 0.8-P2-CN with 1.5 wt% Pt loading showed the highest increase among others. Though, G-CN and 1.6-P1-CN nanosheets possess well improved charge carrier separation abilities through protonation and phosphorus interstitial doping, and their  $\text{H}_2$  evolution rates could greatly enhanced by adding  $\text{K}_2\text{HPO}_4$  to facilitate both proton reduction and the photooxidation of TEOA. However, their limited visible light absorption abilities with a wide bandgap of around 2.7 eV will confine the further improvement of visible-light  $\text{H}_2$  evolution.

In contrast, the 0.8-P2-CN nanosheets could harvest much more visible light to generate photo-excited electrons and holes with a significantly narrowed bandgap of 2.42 eV (ESI, Fig. S7†). Thus, together with the enhanced charge carrier separation, proton reduction and photooxidation of TEOA, the significantly intensified visible-light absorption ability could help the Pt loaded 0.8-P2-CN nanosheets to boost visible-light  $\text{H}_2$  evolution rate to an extremely high level.

In our 25 hours long-term  $\text{H}_2$  evolution experiments, it was found that the Pt loaded 0.8-P2-CN generated nearly the same amount of  $\text{H}_2$  for each 5 hours period in the TEOA solution, while the  $\text{H}_2$  generated in the last 5 hours period could still remain a 76.5% amount of that in the first 5 hours for the optimized TEOA/ $\text{K}_2\text{HPO}_4$  mixture solution. As stated above, the  $\text{K}_2\text{HPO}_4$  would not be consumed during the photocatalytic  $\text{H}_2$  evolution. The gradual decrease of the long-term  $\text{H}_2$  evolution rate in the TEOA/ $\text{K}_2\text{HPO}_4$  solution should be attributed to the significant consumption of TEOA during the photocatalytic  $\text{H}_2$  evolution process. Thus, both the long-term  $\text{H}_2$  evolution experiments conducted in TEOA and TEOA/ $\text{K}_2\text{HPO}_4$  solutions indicated the excellent photocatalytic stability of the  $\text{H}_3\text{PO}_2$  doped nanosheets. The FTIR, elemental analysis conducted using STEM and XPS narrow scan results of the fresh and used 0.8-P2-CN suggest that there are no obvious changes which may induce adverse effect on the photocatalytic performances, confirming the stability of the as-prepared  $\text{g-C}_3\text{N}_4$  nanosheets (ESI, Fig. S10–S12†).

In addition, the spent 0.8-P2-CN catalyst still showed observable  $\text{H}_2$  generation ability (ESI, Video S2†). The 0.8-P2-CN with 1.5 wt% Pt loading achieved an AQY of 10.7% and 40.4% at 420 nm in the TEOA and TEOA/ $\text{K}_2\text{HPO}_4$  (ESI, Fig. S13†), respectively, indicating the extremely efficient visible-light photocatalytic  $\text{H}_2$  evolution over the  $\text{H}_3\text{PO}_2$  doped  $\text{g-C}_3\text{N}_4$  nanosheets compared with the previously reported work (Table S4†). The AQY measurement results at other wavelengths including 400, 450, 500, 550 and 600 nm were also supplemented in the ESI (Fig. S14 and Table S5†).

## Conclusions

Nitrogen deficient and protonated  $\text{g-C}_3\text{N}_4$  nanosheets were successfully synthesized through a one-step, *in situ* reduction



process combining both a  $\text{NH}_4\text{Cl}$ -assisted strategy and  $\text{H}_3\text{PO}_2$  doping. It has been demonstrated that the protonated  $\text{g-C}_3\text{N}_4$  nanosheets have superb photocatalytic activities and can be robustly fabricated by using  $\text{NH}_4\text{Cl}$  as a dynamic gas template. Compared with the  $\text{g-C}_3\text{N}_4$  nanosheets which were simply further protonated by interstitial  $\text{H}_3\text{PO}_4$  doping, the electronic bandgaps of the nitrogen deficient  $\text{g-C}_3\text{N}_4$  nanosheets can be easily controlled by adjusting the added  $\text{H}_3\text{PO}_2$ . The enhanced protonation and reduced electronic bandgaps of  $\text{H}_3\text{PO}_2$  doped  $\text{g-C}_3\text{N}_4$  nanosheets can not only readily harvest visible light but also serve to separate the excited state charge carriers more effectively, thereby offering extremely efficient  $\text{H}_2$  production under visible-light irradiation.

With the addition of  $\text{K}_2\text{HPO}_4$  to TEOA solution, the  $\text{H}_2$  evolution rate over the 1.5 wt% Pt loaded  $\text{H}_3\text{PO}_2$  doped  $\text{g-C}_3\text{N}_4$  nanosheets could be boosted to  $881.7 \mu\text{mol h}^{-1}$  with an apparent quantum yield of 40.4% at 420 nm. In addition, this comprehensive investigation on different phosphorus compounds for  $\text{g-C}_3\text{N}_4$  nanosheets modification indicates that  $\text{H}_3\text{PO}_2$  is a promising dopant to synergistically modify the  $\text{g-C}_3\text{N}_4$  photocatalysts in a single step. We believe this work will provide guidance for the facile synthesis of nitrogen defective and protonated  $\text{g-C}_3\text{N}_4$ -based materials for further synergistic enhancements of visible-light photocatalysts performance.

## Conflicts of interest

There are no conflicts to declare.

## Acknowledgements

The authors acknowledge the financial support from State Key Laboratory of Chemical Engineering (Tianjin University) and EPSRC. We appreciate the valuable suggestions provided by Dr Xiangyu Jie (Chemistry department, University of Oxford) for manuscript preparation. Weisong Li and Litong Jiang also gratefully thank the China Scholarship Council (CSC) for scholarships.

## Notes and references

- G. Liu, T. Wang, H. Zhang, X. Meng, D. Hao, K. Chang, P. Li, T. Kako and J. Ye, *Angew. Chem.*, 2015, **127**, 13561.
- H. Yu, R. Shi, Y. Zhao, T. Bian, Y. Zhao, C. Zhou, G. I. N. Waterhouse, L. Wu, C. Tung and T. Zhang, *Adv. Mater.*, 2017, **29**, 1605148.
- L. Ge, C. Han and J. Liu, *Appl. Catal., B*, 2011, **108**, 100.
- X. Liu, P. Wang, H. Zhai, Q. Zhang, B. Huang, Z. Wang, Y. Liu, Y. Dai, X. Qin and X. Zhang, *Appl. Catal., B*, 2018, **232**, 521.
- G. Zhang, S. Zang, L. Lin, Z. A. Lan, G. Li and X. Wang, *ACS Appl. Mater. Interfaces*, 2016, **8**, 2287.
- P. Niu, L. Zhang, G. Liu and H. M. Cheng, *Adv. Funct. Mater.*, 2012, **22**, 4763.
- X. Lu, K. Xu, P. Chen, K. Jia, S. Liu and C. Wu, *J. Mater. Chem. A*, 2014, **2**, 18924.
- C. Li, S. Yu, H. Dong, C. Liu, H. Wu, H. Che and G. Chen, *Appl. Catal., B*, 2018, **238**, 284–293.
- C. Li, Y. Du, D. Wang, S. Yin, W. Tu, Z. Chen, M. Kraft, G. Chen and R. Xu, *Adv. Funct. Mater.*, 2017, **27**, 1604328.
- C. Li, Y. Xu, W. Tu, G. Chen and R. Xu, *Green Chem.*, 2017, **19**, 882–899.
- Z. Li, C. Kong and G. Lu, *J. Phys. Chem. C*, 2015, **120**, 56.
- Y. P. Zhu, T. Z. Ren and Z. Y. Yuan, *ACS Appl. Mater. Interfaces*, 2015, **7**, 16850.
- P. Niu, G. Liu and H. M. Cheng, *J. Phys. Chem. C*, 2012, **116**, 11013.
- Y. Zhang, A. Thomas, M. Antonietti and X. Wang, *J. Am. Chem. Soc.*, 2008, **131**, 50–51.
- M. Wu, T. Ding, J. Cai, Y. Wang, H. Xian, H. Zhang, Y. Tian, T. Zhang and X. Li, *ACS Sustainable Chem. Eng.*, 2018, **6**, 8167.
- P. Niu, L. C. Yin, Y. Q. Yang, G. Liu and H. M. Cheng, *Adv. Mater.*, 2014, **26**, 8046.
- Z. Hong, B. Shen, Y. Chen, B. Lin and B. Gao, *J. Mater. Chem. A*, 2013, **1**, 11754.
- L. Shi, K. Chang, H. Zhang, X. Hai, L. Yang, T. Wang and J. Ye, *Small*, 2016, **12**, 4431.
- Y. Zhang, T. Mori, J. Ye and M. Antonietti, *J. Am. Chem. Soc.*, 2010, **132**, 6294.
- J. Yuan, Q. Gao, X. Li, Y. Liu, Y. Fang, S. Yang, F. Peng and X. Zhou, *RSC Adv.*, 2014, **4**, 52332.
- M. Groenewolt and M. Antonietti, *Adv. Mater.*, 2005, **17**, 1789.
- Y. Cui, Z. Ding, X. Fu and X. Wang, *Angew. Chem.*, 2012, **124**, 11984.
- W. Lei, D. Portehault, R. Dimova and M. Antonietti, *J. Am. Chem. Soc.*, 2011, **133**, 7121.
- J. Fu, B. Zhu, C. Jiang, B. Cheng, W. You and J. Yu, *Small*, 2017, **13**, 1603938.
- G. Dong, Z. Ai and L. Zhang, *RSC Adv.*, 2014, **4**, 5553.
- J. Sehnert, K. Baerwinkel and J. Senker, *J. Phys. Chem. B*, 2007, **111**, 10671.
- B. Jürgens, E. Irran, J. Senker, P. Kroll, H. Müller and S. Wolfgan, *J. Am. Chem. Soc.*, 2003, **125**, 10288.
- V. W. H. Lau, I. Moudrakovski, T. Botari, S. Weinberger, M. B. Mesch, V. Duppel, J. Senker, V. Blum and B. V. Lotsch, *Nat. Commun.*, 2016, **7**, 12165.
- Y. Fu, J. Zhu, C. Hu, X. Wu and X. Wang, *Nanoscale*, 2014, **6**, 12555.
- S. J. Makowski, D. Gunzelmann, J. Senker and W. Schnick, *Z. Anorg. Allg. Chem.*, 2009, **635**, 2434.
- M. Zhu, S. Kim, L. Mao, M. Fujitsuka, J. Zhang, X. Wang and T. Majima, *J. Am. Chem. Soc.*, 2017, **139**, 13234.
- X. Ma, Y. Lv, J. Xu, Y. Liu, R. Zhang and Y. Zhu, *J. Phys. Chem. C*, 2012, **116**, 23485.
- G. R. Goward, M. F. Schuster, D. Sebastiani, I. Schnell and H. W. Spiess, *J. Phys. Chem. B*, 2002, **106**, 9322.
- T. Emmler, S. Gieschler, H. H. Limbach and G. Buntkowsky, *J. Mol. Struct.*, 2004, **700**, 29.
- Y. Chen, B. Lin, H. Wang, Y. Yang, H. Zhu, W. Yu and J. M. Basset, *Chem. Eng. J.*, 2016, **286**, 339.



- 36 C. Ye, J. X. Li, Z. J. Li, X. B. Li, X. B. Fan, L. P. Zhang, B. Chen, C. H. Tung and L. Z. Wu, *ACS Catal.*, 2015, **5**, 6973–6979.
- 37 M. Rong, Z. Cai, L. Xie, C. Lin, X. Song, F. Luo, Y. Wang and X. Chen, *Chem.–Eur. J.*, 2016, **22**, 9387.
- 38 H. Gao, S. Yan, J. Wang, Y. A. Huang, P. Wang, Z. Li and Z. Zou, *Phys. Chem. Chem. Phys.*, 2013, **15**, 18077.
- 39 K. B. Yatsimirskii, V. V. Nemoskalenko, V. G. Aleshin, Y. I. Bratushko and E. P. Moiseenko, *Chem. Phys. Lett.*, 1977, **52**, 481.
- 40 M. A. Mohamed, M. F. M. Zain, L. J. Minggu, M. B. Kassim, N. A. S. Amin, W. N. W. Salleh, M. N. I. Salehmin, M. F. M. Nasir and Z. A. M. Hir, *Appl. Catal., B*, 2018, **236**, 265.
- 41 J. Liu, T. Zhang, Z. Wang, G. Dawson and W. Chen, *J. Mater. Chem.*, 2011, **21**, 14398.
- 42 G. Zhang, M. Zhang, X. Ye, X. Qiu, S. Lin and X. Wang, *Adv. Mater.*, 2014, **26**, 805.
- 43 W. Tu, Y. Xu, J. Wang, B. Zhang, T. Zhou, S. Yin, S. Wu, C. Li, Y. Huang, Y. Zhou, Z. Zou, J. Robertson, M. Kraft and R. Xu, *ACS Sustainable Chem. Eng.*, 2017, **5**, 7260.
- 44 G. Dong, K. Zhao and L. Zhang, *Chem. Commun.*, 2012, **49**, 6178.
- 45 J. Qin and H. Zeng, *Appl. Catal., B*, 2017, **209**, 161–173.
- 46 F. Wang, Y. Wang, Y. Feng, Y. Zeng, Z. Xie, Q. Zhang, Y. Su, P. Chen, Y. Liu, K. Yao, W. Lv and G. Liu, *Appl. Catal., B*, 2018, **221**, 510–520.
- 47 Y. Zhao, M. Shalom and M. Antonietti, *Appl. Catal., B*, 2017, **207**, 311.
- 48 J. Zhang, M. Zhang, R. Sun and X. Wang, *Angew. Chem., Int. Ed.*, 2012, **51**, 10145.
- 49 G. Liu, G. Zhao, W. Zhou, Y. Liu, H. Pang, H. Zhang, D. Hao, X. Meng, P. Li, T. Kako and J. Ye, *Adv. Funct. Mater.*, 2016, **26**, 6822.

